X-ray spectroscopy with an AlInP photodiode

Article (Accepted Version)

X-ray spectroscopy with an AlInP photodiode

G. Lioliou[1*], S. Butera[1], A.B. Krysa[2], and A.M. Barnett[1]
[1]Space Research Group, Sch. of Engineering and Informatics, University of Sussex, Falmer, Brighton, BN1 9QT, UK
[2]National Epitaxy Facility, University of Sheffield, Mappin Street, Sheffield, S1 3JD, UK

Abstract

A custom-made $Al_{0.52}In_{0.48}P$ p^+-i-n^+ circular mesa X-ray photodiode (200 μm diameter; 2 μm i layer thickness) has been investigated for its use in photon counting X-ray spectroscopy within the energy range 4.95 keV to 21.17 keV. This the widest energy range so far used to characterise an AlInP X-ray detector. High-purity X-ray fluorescence calibration samples were excited by a Mo target X-ray tube to give characteristic energy photons with which to illuminate the detector. X-ray fluorescence spectra were accumulated with the $Al_{0.52}In_{0.48}P$ X-ray detector coupled to a custom-made charge-sensitive preamplifier (both operated at a temperature of 30 °C ± 2 °C). The charge output linearly increased with X-ray photon energy. The energy resolution (*Full Width at Half Maximum, FWHM*) degraded from 0.99 keV ± 0.02 keV (80 e^- rms) at 4.95 keV to 1.12 keV ± 0.02 keV (89 e^- rms) at 21.17 keV. The increase of the *FWHM* with increased energy exceeded the increase expected as a consequence of Fano noise. Hence, the presence of energy dependent incomplete charge collection noise was suggested. The count rate linearly increased with increasing incident X-ray flux across the investigated flux range, up to ~ 3.8×10^5 photons s^{-1} cm^{-2}.

Keywords: Aluminium Indium Phosphide; AlInP; X-ray spectroscopy; photodiode.

1. Introduction

$Al_{0.52}In_{0.48}P$ offers many advantages over other semiconductor materials and as such it has started to attract consideration for use in X-ray spectrometers. It has an indirect bandgap of 2.31 eV [1] which results in fewer carriers to be thermally generated at a given temperature, compared to semiconductors with narrower bandgap; Si, which is the standard choice for X-ray spectrometers in the energy range of interest, has a bandgap of 1.12 eV at 300 K [2]. Higher X-ray quantum detection efficiency per unit thickness is achieved with $Al_{0.52}In_{0.48}P$ compared to many other wide bandgap materials, such as GaAs, AlGaAs, and 4H-SiC, as well as Si, as a result of the presence of In (atomic number 49). As an example, the linear X-ray absorption coefficient is 0.032 μm^{-1} for $Al_{0.52}In_{0.48}P$, 0.019 μm^{-1} for GaAs, and 0.008 μm^{-1} for Si, at 10 keV [3] [4]. Additionally, better radiation hardness may be expected from $Al_{0.52}In_{0.48}P$ [5], compared to other narrower bandgap semiconductors, although extensive radiation hard measurements are yet to be reported for the material. Radiation in a space environment can affect the performance of X-ray detectors, causing degradation [6]; the intensity and origin of space radiation can vary greatly; examples include protons and electrons trapped in the Van Allen belts of Earth; protons, electrons, and heavy ions from Solar flares; electrons and ions in the Jovian magnetosphere. $Al_{0.52}In_{0.48}P$ is the widest bandgap III-V semiconductor material which can be grown lattice matched to GaAs [7]; as such high quality material can be grown on commercially available GaAs substrates. The above advantages motivate the development of $Al_{0.52}In_{0.48}P$ for X-ray spectrometers, which can operate uncooled in room temperature and high temperature environments. Applications of such a spectrometer include space science missions (e.g. in situ analysis and remote sensing of planetary and related surfaces with X-ray fluorescence spectroscopy) as well as terrestrial applications in harsh environments (e.g. monitoring nuclear materials and in situ lubricant analysis for tribological wear in oil lubricated machinery [8]).

Both avalanche [9] and non-avalanche [10][11] $Al_{0.52}In_{0.48}P$ photodiodes for X-ray spectroscopy have been previously reported. Under illumination of an ^{55}Fe radioisotope X-ray source, an energy resolution (*Full Width at Half Maximum, FWHM* at 5.9 keV) of 682 eV was achieved with an avalanche p^+-i-p^--n^+ $Al_{0.52}In_{0.48}P$ (1 μm avalanche region) at room temperature [9]. Non-avalanche $Al_{0.52}In_{0.48}P$ p^+-i-n^+ photodiode detectors (2 μm i layer) have also been investigated under illumination

*Corresponding author. Tel.: +44 (0) 1273 872568. E-mail address: G.Lioliou@sussex.ac.uk

of X-rays of the same energy; for those devices the best energy resolution (*FWHM* at 5.9 keV) reported was 930 eV at room temperature [10] and 1.57 keV at 100 °C [11]. $Al_{0.52}In_{0.48}P$'s average electron hole pair creation energy (in response to illumination with X-ray photons) has also been measured using an ^{55}Fe radioisotope X-ray source; a value of 5.34 eV ± 0.07 eV was found at 20 °C [12]. Indeed, all the previously reported results with $Al_{0.52}In_{0.48}P$ X-ray detectors for photon counting spectroscopy have been limited to their response to illumination with ^{55}Fe radioisotope X-ray sources (such sources give characteristic Mn Kα (5.9 keV) and Mn Kβ (6.49 keV) emission lines [13].

In this paper, the performance of an $Al_{0.52}In_{0.48}P$ X-ray spectrometer is reported as a function of incident X-ray photon energy (4.95 keV to 21.17 keV). The work is important since it has revealed energy dependent effects within the material, namely measurable incomplete charge collection noise, which affects the achievable energy resolution as photon energy increases.

2. X-ray spectrometer design

The reported X-ray spectrometer consisted of a prototype $Al_{0.52}In_{0.48}P$ X-ray detector DC coupled to a custom-made low-noise charge-sensitive preamplifier. An ORTEC 572A shaping amplifier and an ORTEC 927 ASPEC 16k channels Multi-Channel Analyzer (MCA) comprised the rest of the spectrometer's electronics chain. A schematic diagram summarising the different parts of the X-ray spectrometer can be seen in **Fig. 1**.

[Figure 1]

The $Al_{0.52}In_{0.48}P$ epilayer was grown and the $Al_{0.52}In_{0.48}P$ X-ray detector was fabricated to the authors' specifications at the EPSRC National Centre for III-V technologies, Sheffield, UK. It was grown on a commercial (100) n-GaAs:Si substrate by metalorganic vapour phase epitaxy (MOVPE). In order to supress the CuPt-like ordered phase, a growing misorientation of 10° towards <111>A at the epitaxial surface of the substrate was chosen [14]. **TABLE I** summarises the epitaxial layer structure. The highly doped p^+ and n^+ layers each had a relatively small thickness, 0.2 μm and 0.1 μm, respectively, to reduce X-ray photon absorption in those regions. The dopant of the p^+ layer (5×10^{17} cm^{-3}) was Zn; dimethylzinc:trimethylamine ($Zn(CH_3)_2$:$N(CH_3)_3$) adduct was used as the precursor. The dopant of the n^+ layer (2×10^{18} cm^{-3}) was Si; disilane (Si_2H_6) was used as the precursor. The unintentionally doped i layer had a thickness of 2 μm. Circular mesa structures with 200 μm diameter were fabricated; 1:1:1 H_3PO_4:H_2O_2:H_2O solution followed by 10 s in 1:8:80 H_2SO_4:H_2O_2:H_2O solution was employed. An Ohmic rear contact was formed by evaporating 20 nm of InGe and 200 nm of Au on to the rear of the substrate. The Ohmic top contact, which had a quasi-annular shape and covered 45% of the face of the devices, was formed by evaporating 20 nm of Ti and 200 nm of Au on to the p^+ layer. The devices were unpassivated. The layer structure and the top-view of the $Al_{0.52}In_{0.48}P$ X-ray detector can be seen in the drawing in **Fig. 2**.

[TABLE I]

[Figure 2]

The charge sensitive preamplifier was of a feedback resistorless design, similar to that reported by Bertuccio et al. [15]. Eliminating the feedback resistor from the feedback loop of such a preamplifier results in the reduction of its electronic noise [15], and hence provided better energy resolution. The charge sensitive preamplifier, when unloaded, had a noise ≈ 40 e^- rms at 20 °C. The detector's leakage current and photocurrent flows away through the input JFET's Gate to Source junction; the Gate to Source junction is slightly forward biased. The input transistor of the preamplifier was a Vishay Siliconix 2N4416A JFET [16]. The input JFET operating point was at a Gate to Source voltage, $V_{GS} \approx 100$ mV, and Drain to Source Voltage, $V_{DS} \approx 5$ V. The Drain to Source current, I_{DS}, at the operating point was ≤ 10 mA, whereas the JFET's input capacitance, C_i, was ≤ 2 pF. The transconductance, g_m, was ≈ 4 mS.

The ORTEC 572A shaping amplifier was set to a fine gain of 1.437, a coarse gain of 50, and a shaping time of 10 μs. A shaping time of 10 μs was found to be the optimum available shaping time (i.e. resulting in the best energy resolution) for an X-ray spectrometer employing a similar $Al_{0.52}In_{0.48}P$ X-ray detector within the temperature range 40 °C to -20 °C [11]. The active filter network of the shaping amplifier provided Semi-Gaussian pulse shaping with a peaking time of 2.2 times of the shaping time. The properties of the charge sensitive preamplifier and shaping amplifier are summarized in **Table II**.

[TABLE II]

3. Experimental results

3.1. X-ray detector electrical characterization

In order to electrically characterize the X-ray detector, its dark current and capacitance were measured at 20 °C and 40 °C, thus more than encompassing the range of temperatures that would be encountered during X-ray spectra accumulation (30 °C ± 2 °C rms deviance). The detector was installed inside a light-tight Al enclosure, which was placed inside a TAS climatic cabinet for temperature control. The detector was left to stabilize 30 minutes at each temperature prior to the measurements, in order to ensure thermal equilibrium. A dry environment (< 5 % relative humidity) was maintained throughout the measurements by flowing dry N_2 inside the climatic cabinet continually. This was done in order to eliminate any humidity related effects. The maximum reverse bias of the X-ray detector was -30 V, corresponding to an applied electric field of 150 kV/cm. This is higher than is typically applied electric fields for many similar semiconductor X-ray detectors (e.g. 103 kV/cm in SiC [17] and 50 kV/cm in GaAs [18]).

The dark current was measured using a Keithley 6487 Picoammeter/Voltage Source, the uncertainty associated with the measurement was 0.3% of the reading plus 400 fA [19]. The leakage current of the TO-5 package itself was also measured as a function of bias at 20 °C and 40 °C; the leakage current of the package was found to be less than that which was measurable with picoammeter; hence its leakage current contribution was regarded as negligible. The forward and reverse dark current of the detector at 20 °C and 40 °C can be seen in **Fig. 3**.

[Figure 3]

The saturation current, I_0, and the ideality factor, n, of the $Al_{0.52}In_{0.48}P$ photodiode detector were extracted from the semi logarithm current, I_F, as a function of applied forward bias, V_{AF}, measurements, since

$$I_F = I_0 e^{\left(\frac{qV_F}{nkT}\right)}, \quad (1)$$

where q is the charge of an electron, k is the Boltzmann constant, and *T* is temperature in K [20]. The saturation current is an important device parameter since it defines the reverse (leakage) current and influences part of the noise of the X-ray spectrometer; the reverse current is either equal (in the ideal case) or proportional to the saturation current, in the absence of surface effects [21]. The saturation current was found to be 7.9×10^{-21} A ± 0.4×10^{-21} A at 20 °C, and 2.1×10^{-19} A ± 0.1×10^{-19} A at 40 °C. The ideality factor was found to not vary within the investigated temperature range; it was measured to be 1.780 ± 0.003 at 20 °C and 1.774 ± 0.004 at 40 °C. Since the ideality factors were between 1 and 2, they suggested that the diffusion and the recombination currents were comparable [21]. The leakage current of the detector at the maximum applied reverse bias, -30 V (internal electric field strength = 150 kV/cm) increased from 0.3 pA ± 0.4 pA (1 nA/cm^2 ± 1 nA/cm^2) at 20 °C to 0.9 pA ± 0.4 pA (3 nA/cm^2 ± 1 nA/cm^2) at 40 °C. The spectroscopic measurements reported in section **3.2. Response linearity measurements of the X-ray spectrometer** were made at -20 V reverse bias. In this bias condition, the leakage current was ≤ 0.6 pA at both temperatures.

The capacitance of the $Al_{0.52}In_{0.48}P$ X-ray detector was measured using an HP 4275A Multi-Frequency LCR meter with 50 mV rms magnitude and 1 MHz frequency test signal; the uncertainty associated with the capacitance reading was (0.1% + 3 fF) × 1.2 [22]. Reverse bias was applied to the detector using a Keithley 6487 Picoammeter/Voltage Source with an uncertainty in the applied bias of 0.1% of the selected bias plus 4 mV [19]. The uncertainty for all the reported absolute values of capacitance was estimated to be ± 0.04 pF, whereas, the uncertainty associated with relative capacitances changes with temperature was estimated to be ± 0.005 pF. The capacitance of the TO-5 package was also measured and was found to be 0.73 pF ± 0.04 pF within the investigated bias and temperature range. The capacitance of the detector (excluding its package) can be seen in **Fig. 4**.

[Figure 4]

The capacitance of the detector was measured to be 1.624 pF ± 0.005 pF at 20 °C, and 1.631 pF ± 0.005 pF at 40 °C, when no external bias was applied. The capacitance of the detector decreased with increasing applied bias, up to -15 V, where the capacitance saturated for further (magnitude) increases in applied reverser bias, suggesting full depletion. The capacitance of the detector at 20 °C (and 40 °C) was measured to be 1.594 pF ± 0.005 pF (and 1.598 pF ± 0.005 pF) at -15 V applied bias and 1.582 pF ± 0.005 pF (and 1.588 pF ± 0.005 pF) at -30 V applied bias. At such biases (-15 V to -30 V), there was no variation of capacitance between the temperatures, within the uncertainty of the measurement. The combined capacitance of the detector and its package when a reverse bias of -20 V was applied, was measured to be 2.32 pF ± 0.04 pF at 20 °C, and 2.33 pF ± 0.04 pF at 40 °C. The depletion width of the detector was calculated using the capacitance measurements (excluding the package) and assuming a parallel plate capacitance [21]; it is presented **Fig. 5**. A relative permittivity of 11.25 for $Al_{0.52}In_{0.48}P$ [7] was used for the depletion width calculation. The depletion width increased as the applied reverse bias increased, up to -15 V, where the detector was found to be fully depleted at both 20 °C and 40 °C. The apparent increase in depletion width (**Fig. 5**) when the applied reverse bias increased, in magnitude, from -15 V to -30 V, was considered to be within the uncertainties of the measurements. As an example, the depletion layer width was calculated to be 1.958 μm ± 0.009 μm and 1.971 μm ± 0.009 μm at -15 V and -30 V applied reverse bias, respectively at 20 °C. The depletion width was 1.98 μm ± 0.05 μm at 20 °C, and 1.97 μm ± 0.05 μm at 40 °C. Considering that the extension of the depletion region to the p^+ and n^+ layers was negligible (the doping concentrations of the p^+ and n^+ layers were higher compared to that of the i layer), this measured width can be said to represent the full i layer width. A thickness of 1.98 μm ± 0.05 μm as determined from these capacitance measurements is consistent with the 2 μm thickness indicated from measurements made during epitaxial growth.

[Figure 5]

3.2. Response linearity measurements of the X-ray spectrometer

The detector was connected to the input of a custom-made, single-channel charge-sensitive preamplifier. The X-ray detector and preamplifier were installed in a custom Al enclosure. The Al enclosure was then installed within a LD Didactic GmbH X-ray apparatus (part number 554 801) with a Mo target X-ray tube (part number 554 861). A custom-made Al collimator lined with PTFE (to absorb all fluorescence from the Al of the collimator) was used to collimate the X-rays from the Mo target X-ray tube. A 4 μm Al foil window in the Al enclosure allowed X-ray to impinge on the detector with minimum attenuation whilst preventing all visible and UV illumination of the detector. The Al enclosure was attached to the goniometer of the apparatus for precise positioning. The output of the preamplifier was shaped by an ORTEC 572A shaping amplifier. The output of the shaping amplifier was connected to an ORTEC 927 ASPEC multi-channel analyser (MCA) for digitation.

Eight high-purity X-ray fluorescence samples were in turn excited by the Mo target X-ray tube; X-ray spectra were accumulated using the $Al_{0.52}In_{0.48}P$ detector X-ray spectrometer. The X-ray fluorescence calibration samples used were V (Kα at 4.95 keV), Cr (Kα at 5.41 keV), Mn (Kα at 5.9 keV), Cu (Kα at 8.04 keV), Zn (Kα at 8.63 keV), Ge (Kα at 9.88 keV), Nb (Kα at 16.61 keV), and Pd (Kα at 21.17 keV) [23]. Each X-ray fluorescence calibration sample was positioned on the sample stand at 45° to the collimator. The X-ray detector-preamplifier system was positioned at 135° to the collimator. This configuration maximized detection of the fluorescence X-ray from the calibration samples and minimized detection of X-rays from the Mo target X-ray tube. The temperature of the X-ray detector-preamplifier system varied from 26 °C to 33 °C, with a mean value of 30 °C ± 2 °C (rms deviance).

The linearity measurements conducted included energy linearity and X-ray intensity linearity. Details of the measurements and the results are presented in the following paragraphs.

3.2.1. Energy linearity

The detected charge response as a function of incident X-ray photon energy was investigated for the reported X-ray spectrometer. The X-ray tube voltage and current were set to their maximum values, 35 kV and 1 mA, respectively. X-ray fluorescence spectra of all the calibration foils were accumulated; the X-ray detector was biased at -20 V and the shaping time was set to 10 μs. The live time for each the accumulated X-ray spectrum was 8 hours.

Gaussians were fitted to the peaks of the accumulated spectra; the centroid channel number of the Kα peak of each foil along with their accepted energy were used to energy calibrate the spectroscopic system. The centroid MCA channel number as a function of energy, for the spectrometer employing the $Al_{0.52}In_{0.48}P$ X-ray detector, can be seen in **Fig. 6**. The line of best fit was calculated using linear least squares fitting. The error bars associated with the fitting for each data point, calculated to be $\leq \pm$ 2 channels, were comparable with the analytical uncertainties in experimentally determining the centroid channel number of each photopeak (typically ± 3 channels). Hence, the voltage output of the spectrometer had a linear relationship with incident photon energy. The residuals of the fit were calculated in percentage terms, and were found to be $\leq \pm$ 0.2 % (± 0.07 % mean).

[Figure 6]

The relationship presented in **Fig. 6** was used to energy calibrate the MCA's charge scale of the accumulated spectra; an example X-ray fluorescence spectrum, of the Mn calibration foil, obtained using the spectrometer, can be seen in **Fig. 7 (a)**. The Mn Kα (at 5.9 keV) and Mn Kβ (at 6.49 keV) lines [23] were not individually resolved, hence the detected X-ray photopeak was the combination of the Mn Kα and Mn Kβ lines. Gaussians were fitted to the peaks in each spectrum (e.g. Mn photopeak seen in **Fig. 7 (a)**) taking into account the appropriate emission ratios [23] and the relative quantum

efficiencies of the detector at the corresponding X-ray energies. Although the MCA low energy cut-off was set at ~2.1 keV to eliminate counts of the zero energy noise peak of the spectrometer, a small portion of the right hand side of its tail can be seen in **Fig. 7 (a)**. The low energy, < 5 keV, tailing seen in **Fig. 7 (a)** was attributed to the combination of counts from partial charge collection of charge created in the non-active layers of the detector and counts due to continuum processes of the X-ray tube. The accumulated X-ray fluorescence spectrum of the Pd calibration foil can be seen in **Fig. 7 (b)**. The Pd Kα (21.17 keV) and Pd Kβ (23.81 keV) lines were individually resolved. The low energy tailing seen in Fig. 7 (b) was attributed to counts from partial charge collection of charge created in the non-active layers on the detector superimposed on the Mo target X-ray tube spectrum.

[Figure 7]

The energy resolution of the spectrometer, quantified as the *FWHM* of the photopeaks in the accumulated spectra, was measured as a function of energy and can be seen in **Fig. 8**. The equivalent noise charge (*ENC*) in e^- rms can also be seen in the same figure. The *FWHM* increased from 0.99 keV ± 0.02 keV (80 e^- rms) at 4.95 keV to 1.12 keV ± 0.02 keV (89 e^- rms) at 21.17 keV. The energy resolution, ΔE, of an X-ray spectrometer, consisting of a non-avalanche photodiode detector coupled to a charge sensitive preamplifier, is degraded due to Fano noise, electronic noise [24], and incomplete charge collection noise, such that,

$$\Delta E \text{ [keV]} = 2.355\sqrt{F\omega E + \left(\frac{\sigma_e}{2.355}\right)^2 + a_1 E^{a_2}}. \quad (2)$$

The first term under the square root is the Fano noise, the second term is the electronic noise with an *ENC* of σ_e in e^- rms, and the third term is the incomplete charge collection noise [25]. The Fano noise is material and energy, *E*, dependent; it can be calculated only if the Fano factor, *F*, and the electron-hole pair creation energy, ω, are known for that material. Since the Fano factor of $Al_{0.52}In_{0.48}P$ has not been reported yet, the Fano factor of another wide bandgap semiconductor, $In_{0.5}Ga_{0.5}P$ (= 0.13 [26]) was used to provide an indicative value. The electron-hole pair creation energy of $Al_{0.52}In_{0.48}P$ was measured to be 5.31 eV at 30 °C [12]. The electronic noise is comprised of the white parallel noise, white series noise (including the induced gate current noise), 1/*f* noise, and dielectric noise [24].

Initially, the third term under the square root (i.e. incomplete charge collection noise) was considered to be negligible. Assuming the measured *FWHM* at 4.95 keV (= 0.99 keV) was the quadratic sum of the electronic noise and Fano noise, i.e. given by Eq. (2) with $a_1 = a_2 = 0$, an electronic noise contribution of 986 eV (79 e^- rms) was calculated. The expected *FWHM* as a function of energy was then calculated from the quadratic sum of the electronic noise and the energy dependent Fano noise. This can be seen in **Fig. 8**. However, the experimentally observed increase in *FWHM* as a function of increased photon energy cannot be solely attributed to the increasing Fano noise. A value of 1.12 keV at 21.17 keV was measured whereas 1.04 keV *FWHM* at 21.17 keV was predicted.

The discrepancy between the measured and predicted *FWHM* as a function of energy (see **Fig. 8**) suggested that the initial assumptions might not have been valid. The contribution of incomplete charge collection noise cannot be assumed negligible, especially at high energies. It should be noted here also that the assumption that the Fano factor of $Al_{0.52}In_{0.48}P$ was the same as that of $In_{0.5}Ga_{0.5}P$ (= 0.13) might have also contributed to the observed discrepancies of **Fig. 8**.

[Figure 8]

Assuming a Fano factor of 0.13, but this time, taking into account the contribution of the incomplete charge collection noise, Eq. (2) was fitted to the measured *FWHM* as a function of energy. The electronic noise, with an *ENC* of σ_e in e^- rms, and the semi-empirical constants of the incomplete charge collection noise, α_1 and α_2, were determined by best-fitting. **Fig. 9** shows the fitting of Eq. (2) to the measured *FWHM* as a function of energy, along with the deduced from the fitting electronic and incomplete charge collection noise contributions. The residuals of the fitting to the measured

FWHM were ≤ 9 eV (≤ 1%). The best-fit electronic noise was 78 e^- rms (979 eV), whereas the semi-empirical constants of the incomplete charge collection noise were found to be $a_1 = 2.8 \times 10^{-6}$ and $a_2 = 2.34$. The incomplete charge collection noise was found to increase from 7 e^- rms at 4.95 keV to 36 e^- rms at 21.17 keV. Fitting Eq. (2) to the measured *FWHM* suggested that the electronic noise would be likely to dominate the energy resolution up to 40 keV, whereas incomplete charge collection noise is predicted to dominate for X-ray energies > 40 keV. However, it should be noted that this is an extrapolation since the measurements reported here used photons with a maximum energy of 21.17 keV. Strictly speaking, the incomplete charge collection noise is non-Gaussian, and hence its contribution is expected to result in a non-symmetric photopeak (in many cases, this can be approximated as a broader Gaussian for the left hand – low energy – side of the photopeak) or even a bifurcated photopeak [25]. Nevertheless, when the incomplete charge collection noise is relatively small compared with the other noise sources present, the incomplete charge collection noise can be approximated to be Gaussian noise source, similar to those for the Fano noise and electronic noise [27]. In the case of the presently reported detectors, since the incomplete charge collection noise was relatively small (36 e^- rms at 21.17 keV) compared with the combination of the other noise sources (82 e^- rms), the incomplete charge collection noise was considered to be adequately described as a Gaussian source, and thus it was considered as contributing to the overall broadening of the photopeak. If the other noise sources had been smaller, or if the incomplete charge collection noise had been larger, as would be expected at higher X-ray energies, this approximation may have been inappropriate. However, the suitability of the common approximation in the present case is demonstrated by the relative morphological similarity of the high and low energy sides of the experimentally-obtained photopeaks.

The fitting of Eq. (2) to the measured *FWHM* as a function of photon energy is not sensitive upon the value of Fano factor used. The extracted parameters of the fitting, for Fano factor values of 0.11, 0.12, 0.13, 0.14, and 0.15, were $\sigma_e = 78.2$ e^- rms ± 0.2 e^- rms, $a_1 = 2.6 \times 10^{-6} \pm 0.2 \times 10^{-6}$ and $a_2 = 2.34 \pm 0.01$. This highlights that an accurate (and usefully precise) extraction of the Fano factor from experimental data that is strongly influenced by electronic and incomplete charge collection noise is difficult [28]. In the present case, it would be impossible. As such, despite the attraction of using the multi-energy measurements to estimate the Fano factor, we refrain from doing so with the present $Al_{0.52}In_{0.48}P$ material.

[Figure 9]

The white parallel noise, ENC_{WP}, arising from the leakage current, and the white series noise, ENC_{WS}, arising from the capacitance, contributions of the $Al_{0.52}In_{0.48}P$ detector were calculated as per Lioliou & Barnett [24], for an applied detector bias of -20 V and a shaping time of 10 μs. The ENC_{WP} was calculated to be ≤ 17 e^- rms for the packaged detector operating at 30 °C ± 2 °C. The ENC_{WS} was calculate to be 6 e^- rms for the packaged detector.

3.2.2. X-ray intensity linearity

The linearity of the spectroscopic system in terms of detected count rate as a function of incident X-ray flux was investigated by varying the current of the X-ray tube. X-ray fluorescence spectra of the Zn (8.63 keV) and Nb (16.61 keV) calibration foils were accumulated. The Mo target X-ray tube current, X_C, was varied from 0.2 mA to 1.0 mA, in 0.2 mA steps. Gaussians were fitted to each of the Kα photopeaks of Zn and Nb in the accumulated spectra. The detected count rate, as defined by the number of counts within the Gaussians fitted to each of the Kα photopeaks of Zn (8.63 keV) and Nb (16.61 keV) over the spectrum accumulation times, in units of counts s^{-1}, was determined as functions of X-ray tube current. The results are presented in **Fig. 10**.

[Figure 10]

Linear relationships were found between the count rate within the Kα photopeaks of Zn and Nb and the X-ray tube current. The lines of best fit were calculated using linear least squares fitting and can

be seen in **Fig. 10**. The response of the spectrometer was found to be linear at detected count rates from 2 counts s^{-1} (7×10^3 counts s^{-1} cm^{-2}) to 11 counts s^{-1} (34×10^3 counts s^{-1} cm^{-2}) at 8.63 keV, and from 0.4 counts s^{-1} (1×10^3 counts s^{-1} cm^{-2}) to 2 counts s^{-1} (7×10^3 counts s^{-1} cm^{-2}), at 16.61 keV.

The incident photon fluxes can be estimated from the detected count rates and the quantum efficiency of the detector at the corresponding X-ray photon energy. The quantum detection efficiency,

$$QE = [\prod_m \exp(-\mu_m x_m)][1 - \exp(-\mu_{AL} x_{AL})], \quad (3)$$

takes into account the linear attenuation coefficient, μ_m, and the thickness, x_m, of the m^{th} dead layer (Au/Ti contact, and GaAs buffer layer), as well as the linear absorption coefficient, μ_{AL}, and the thickness, x_{AL}, of the active layer ($Al_{0.52}In_{0.48}P$ p^+ layer and i layer) [29]. The linear absorption coefficient of $Al_{0.52}In_{0.48}P$ was calculated as a function of energy using the elemental (Al, In, and P) linear absorption coefficients [3] and the elements' appropriate weight fractions [4]. The linear X-ray absorption coefficient as a function of energy for $Al_{0.52}In_{0.48}P$ and Si [3] for comparison purposes, is presented in **Fig. 11**. The *QE* was calculated to be 0.101 at 8.63 keV and 0.0174 at 16.61 keV. The detected count rates corresponded to incident fluxes ranging from 0.7×10^5 photons s^{-1} cm^{-2} to 3.3×10^5 photons s^{-1} cm^{-2} at 8.63 keV, and from 0.8×10^5 photons s^{-1} cm^{-2} to 3.8×10^5 photons s^{-1} cm^{-2} at 16.61 keV.

[Figure 11]

4. Conclusions

An X-ray spectrometer employing an $Al_{0.52}In_{0.48}P$ detector was investigated for its suitability for photon counting X-ray spectroscopy within the energy range 4.49 keV and 21.17 keV. The spectrometer was operated uncooled at 30 °C ± 2 °C. The detector was initially electrically characterized, and then coupled to the spectrometer electronics, consisting of a custom-made charge-sensitive preamplifier, a shaping amplifier, and an MCA. X-ray fluorescence spectra of high-purity calibration samples were accumulated to study the linearity of the spectrometer.

X-ray calibration samples were fluoresced by a Mo target X-ray tube and spectra were accumulated. A linear relationship between the spectrometer charge output and photon energy was found across the energy range 4.49 keV and 21.17 keV. This is the widest energy range so far used to investigate an AlInP X-ray spectrometer. The *FWHM* degraded from 0.99 keV ± 0.02 keV (80 e^- rms) at 4.95 keV to 1.12 keV ± 0.02 keV (89 e^- rms) at 21.17 keV. The experimentally observed broadening of the *FWHM* with increased energy could not be attributed only to increasing Fano noise; significant contribution of incomplete charge collection noise especially at high energies, was suggested. This is the first time incomplete charge trapping noise has been found in an AlInP X-ray spectrometer. Assuming a Fano factor of 0.13 (i.e. equal to that for $In_{0.5}Ga_{0.5}P$ [26]), the incomplete charge collection noise was found to increase from 7 e^- rms at 4.95 keV to 36 e^- rms at 21.17 keV and to be the dominant source of noise for X-ray energies > 40 keV. The detected count rate was found to linearly depend on the incident X-ray flux across the investigated flux ranges for photon energies of 8.63 keV and 16.61 keV.

Investigation of the X-ray performance of thicker $Al_{0.52}In_{0.48}P$ detectors (i layer thickness > 2 μm), with increased X-ray quantum detection efficiency, is anticipated as part of future work. Other further work, including characterisation of such detectors under the illumination of hard X-rays and γ-rays, is also planned. As is quantification of any incomplete charge collection noise and its energy dependence at such high photon energies.

ACKNOWLEDGEMENTS

This work was supported in part by the Engineering and Physical Sciences Research Council, United Kingdom, through grant EP/P021271/1 (A.M.B., PI) and Science and Technology Facilities Council, united Kingdom, through grant ST/M002772/1 (A.M.B., PI). A.M.B. acknowledges funding from the

Leverhulme Trust, United Kingdom, in the form of a 2016 Philip Leverhulme Prize. The authors are grateful to R. J. Airey and S. Kumar at the University of Sheffield EPSRC National Epitaxy Facility for device fabrication.

DATA AVAILABILITY

Data underlying this work are subject to commercial confidentiality. The Authors regret that they cannot grant public requests for further access to any data produced during the study, however the key findings are fully included within the article.

REFERENCES

[1] J.S. Cheong, J.S.L. Ong, J.S. Ng, A.B. Krysa, and J.P.R. David, IEEE J. Sel. Top. Quantum Electron. **20**, 2014, 142.
[2] W. Bludau, A. Onton, and W. Heinke, J. Appl. Phys. **45**, 1974, 1846.
[3] J.H. Hubbell, Int. J. Appl. Radiat. **33**, 1982, 1269.
[4] R. Jenkins, R.W. Gould and D. Gedcke, 2nd ed., Quantitative X-ray Spectrometry Marcel Dekker; 1995.
[5] Y. Zhang, C. Li, Y. Gu, K. Wang, H. Li, X. Shao, and J. Fang, IEEE Photon. Tech. L. **22**, 2010, 944.
[6] A.F. Abbey, P.J. Bennie, M.J.L. Turner, B. Altieri, and S. Rives, Nucl. Instrum. Meth. Phys. Res. A **513**, 2003, 136.
[7] J.S.L. Ong, J.S. Ng, A.B. Krysa, and J.P.R. David, IEEE Electr. Device L. **32**, 2011, 1528.
[8] J. Lees, D. Bassford, and A.M. Barnett, (University of Sussex, UK), US10151717, 2018.
[9] A. Auckloo, J.S. Cheong, X. Meng, C.H. Tan, J.S. Ng, A.B. Krysa, R.C., Tozer, J.P.R. David, J. Instrum. **11**, 2016, P03021.
[10] S. Butera, G. Lioliou, A.B. Krysa and A.M. Barnett, J. Appl. Phys. **120**, 2016, 024502.
[11] S. Butera, T. Gohil, G. Lioliou, A.B. Krysa and A.M. Barnett, J. Appl. Phys. **120**, 2016, 174503.
[12] S. Butera, G. Lioliou, A.B. Krysa and A.M. Barnett, Nucl. Instrum. Meth. Phys. Res. A **879**, 2018, 64.
[13] U. Schötzig, Appl. Radiat. Isot. **53**, 2000, 469.
[14] M.P. Halsall, A.D.F. Dunbar, and U. Bangert, J. Appl. Phys. **85**, 1999, 199.
[15] G. Bertuccio, P. Rehak, and D. Xi, Nucl. Instrum. Meth. Phys. Res. A **326**, 1993, 71.
[16] Siliconix, 2N4416/2N4416A/SST4416 N-Channel JFETs, Data Sheet, 70242 S-04028, Rev. F, 04-Jun-01 Vishay Electronic GmbH; 2001.
[17] G. Bertuccio, S. Caccia, D. Puglisi, and D. Macera, Nucl. Instrum. Meth. Phys. Res. A **652**, 2011, 193.
[18] G. Lioliou, M.D.C. Whitaker, and A.M. Barnett, J. Appl. Phys. **122**, 2017, 244506.
[19] Keithley Instruments, Inc., Model 6487 Picoammeter/Voltage Source Reference Manual, 6487-901-01 Rev C Ohio; 2011.
[20] G. Lioliou, X. Meng, J.S. Ng and A.M. Barnett, J. Appl. Phys. **119**, 2016, 124507.
[21] S.M. Sze, and K.K. Ng, 3rd ed., Physics of Semiconductor Devices, John Wiley & Sons New Jersey; 2007.
[22] Hewlett Packard, Model HP 4275A Multi-Frequency LCR Meter Operating Manual, 04275-90004 Tokyo; 1979.
[23] M. Sánchez del Rio, A. Brunetti, B. Golosio, A. Somogyi, and A. Simionovici, XRAYLIB Tables (X-ray Fluorescence Cross-Section) European Synchrotron Radiation Facility and University of Sassari; 2003.
[24] G. Lioliou and A.M. Barnett, Nucl. Instrum. Meth. Phys. Res. A **801**, 2015, 63.
[25] C. Erd, A. Owens, G. Brammertz, M. Bavdaz, A. Peacock, V. Lämsä, S. Nenonen, H. Andersson and N. Haack, Nucl. Instrum. Meth. Phys. Res. A **487**, 2002, 78.
[26] G. Lioliou, A.B. Krysa, and A.M. Barnett, J. Appl. Phys. **124**, 2018, 195704.
[27] A. Owens, Compound semiconductor radiation detectors, Taylor & Francis Group Florida; 2012.
[28] M. Sammartini, M. Gandola, F. Mele, B. Garavelli, D. Macera, P. Pozzi and G. Bertuccio, Nucl. Instrum. Meth. Phys. Res. A **910**, 2018, 168.
[29] G.W. Fraser, X-ray Detectors in Astronomy Cambridge University Press; 1989.

Table and Figures captions

TABLE I. Layer structure of the $Al_{0.52}In_{0.48}P$ p^+-i-n^+ wafer.

TABLE II. Summary of important properties of the experimental set up.

Fig. 1. Schematic diagram of the different parts comprising the X-ray spectrometer.

Fig. 2. (a) Layer structure (not in scale) and (b) the top-view of the $Al_{0.52}In_{0.48}P$ X-ray detector.

Fig. 3. Current as a function of (a) forward and (b) reverse applied bias of the $Al_{0.52}In_{0.48}P$ X-ray detector at 40 °C (filled diamonds) and 20 °C (open squares). Even though the current was measured every 0.01 V for forward bias and every 1 V for reverse bias, data points are only shown for 0.1 V steps for forward bias and 2 V steps for reverse bias to improve the clarity of the figure.

Fig. 4. Capacitance as a function of reverse applied bias of the $Al_{0.52}In_{0.48}P$ X-ray detector at 40 °C (filled diamonds) and 20 °C (open squares). Even though the capacitance was measured every 1 V for reverse applied bias, data points are only shown for 2 V steps to improve the clarity of the figure.

Fig. 5. Calculated detector depletion width as a function of applied reverse bias at 40 °C (× sign) and 20 °C (filled circle). Even though the depletion width was calculated every 1 V for reverse applied bias, data points are only shown for 2 V steps to improve the clarity of the figure.

Fig. 6. Centroid MCA channel number (open triangles) as a function of energy for the spectrometer employing the $Al_{0.52}In_{0.48}P$ X-ray detector. The line of best fit, as calculated using linear least squares fitting and the residuals of the fit, in percentage terms, (+ symbols), can also be seen.

Fig. 7. (a) Mn spectrum and (b) Pd spectrum accumulated with spectrometer employing the $Al_{0.52}In_{0.48}P$ X-ray detector. The MCA's charge scale of the spectra was energy calibrated using the relationship presented in **Fig. 6**.

Fig. 8. Measured *FWHM* (open circles) and quadratic sum of electronic and Fano noise (dotted line) as a function of X-ray photon energy of the spectrometer employing the $Al_{0.52}In_{0.48}P$ X-ray detector. The individual components of the energy resolution, Fano (dashed dotted line) and electronic (dashed line), are also shown.

Fig. 9. Measured *FWHM* (open circles) and Eq. (1) fitted to the measured *FWHM* (dotted line) as a function of X-ray photon energy of the spectrometer employing the $Al_{0.52}In_{0.48}P$ X-ray detector. The individual components of the energy resolution, Fano (dashed dotted line), electronic (dashed line), and incomplete charge collection (solid line), are also shown.

Fig. 10. Detected count rate within the Gaussian fitted to the Zn Kα peak (8.63 keV) (open diamonds) and Nb Kα peak (16.61 keV) (stars) as a function of X-ray tube current. The lines of best fit, as calculated using linear least squares fitting, can also be seen.

Fig. 11. The linear absorption coefficient of $Al_{0.52}In_{0.48}P$ (solid line) and Si (dashed line) as a function of X-ray energy.

Figure 1

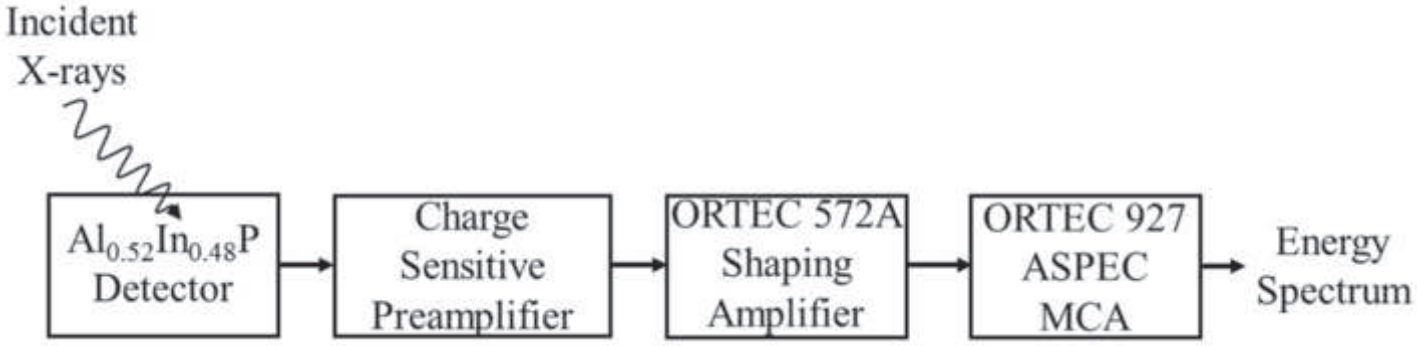
Incident
X-rays
$Al_{0.52}In_{0.48}P$
Detector
Charge
Sensitive
Preamplifier
ORTEC 572A
Shaping
Amplifier
ORTEC 927
ASPEC
MCA
Energy
Spectrum

Figure 2

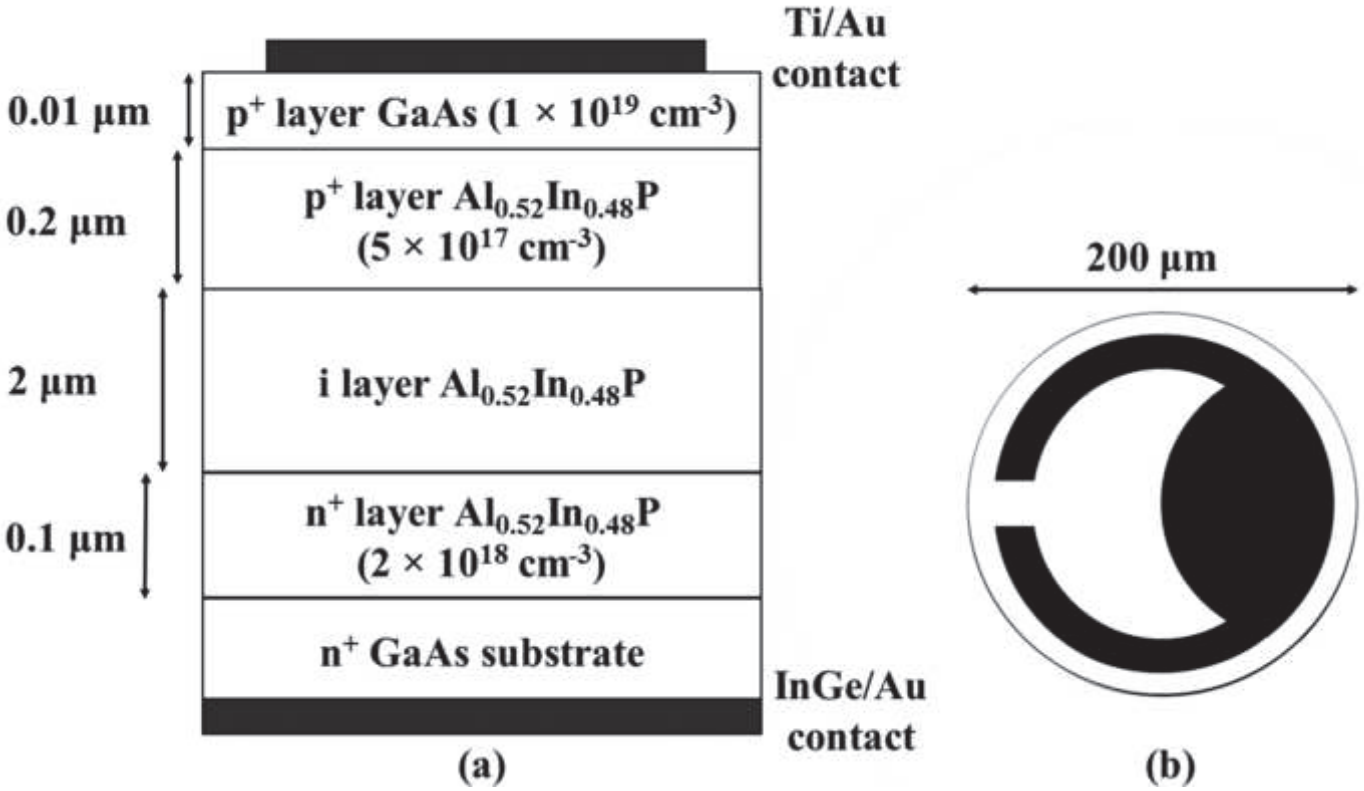
Ti/Au
contact
0.01 µm
p+ layer GaAs (1 × 10^19 cm^-3)
0.2 µm
p+ layer Al0.52In0.48P
(5 × 10^17 cm^-3)
2 µm
i layer Al0.52In0.48P
0.1 µm
n+ layer Al0.52In0.48P
(2 × 10^18 cm^-3)
n+ GaAs substrate
InGe/Au
contact
(a)
200 µm
(b)

Figure 3a

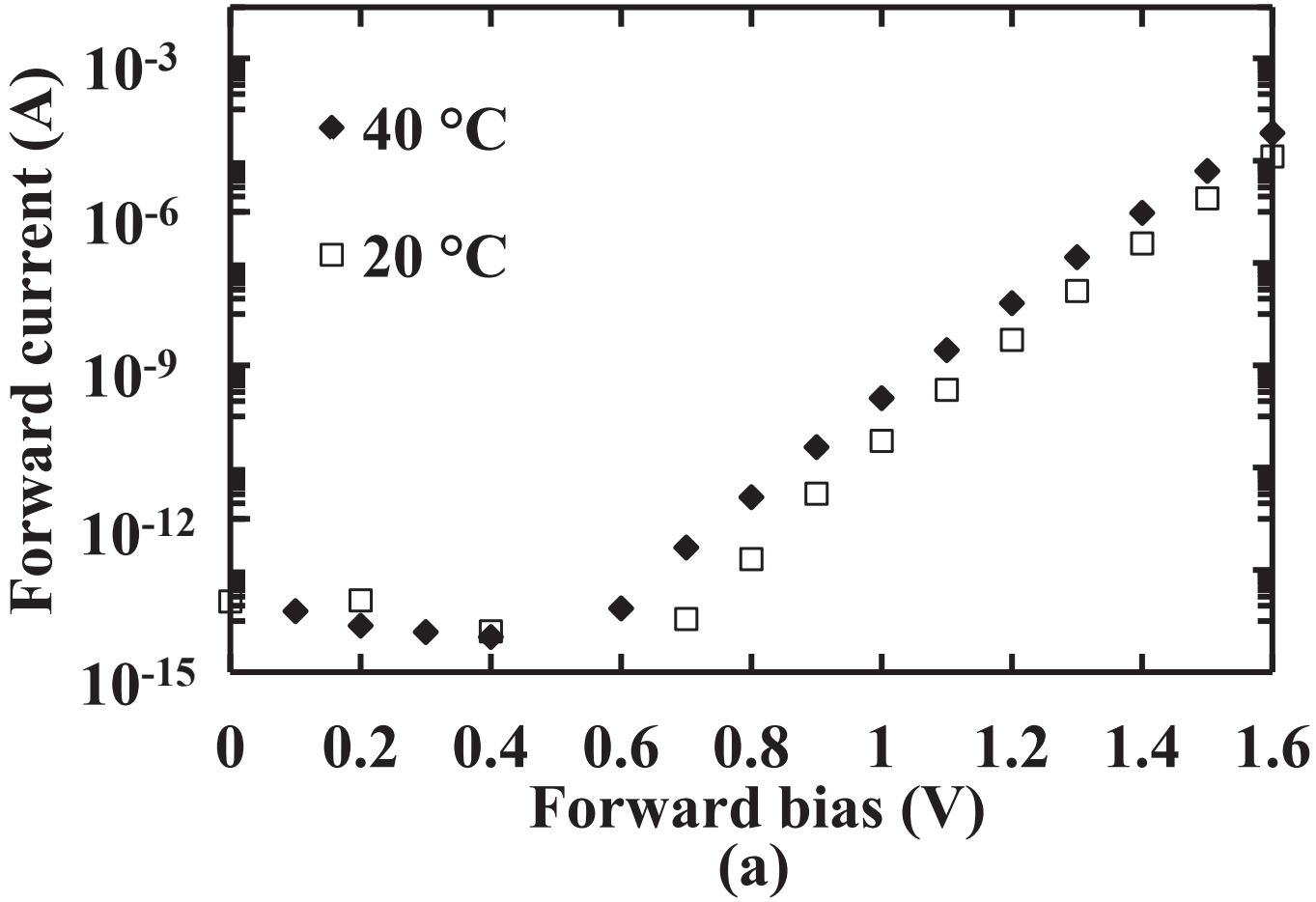
Forward current (A)
10-3
10-6
10-9
10-12
10-15
40 °C
20 °C
0
0.2
0.4
0.6
0.8
1
1.2
1.4
1.6
Forward bias (V)
(a)

Figure 3b

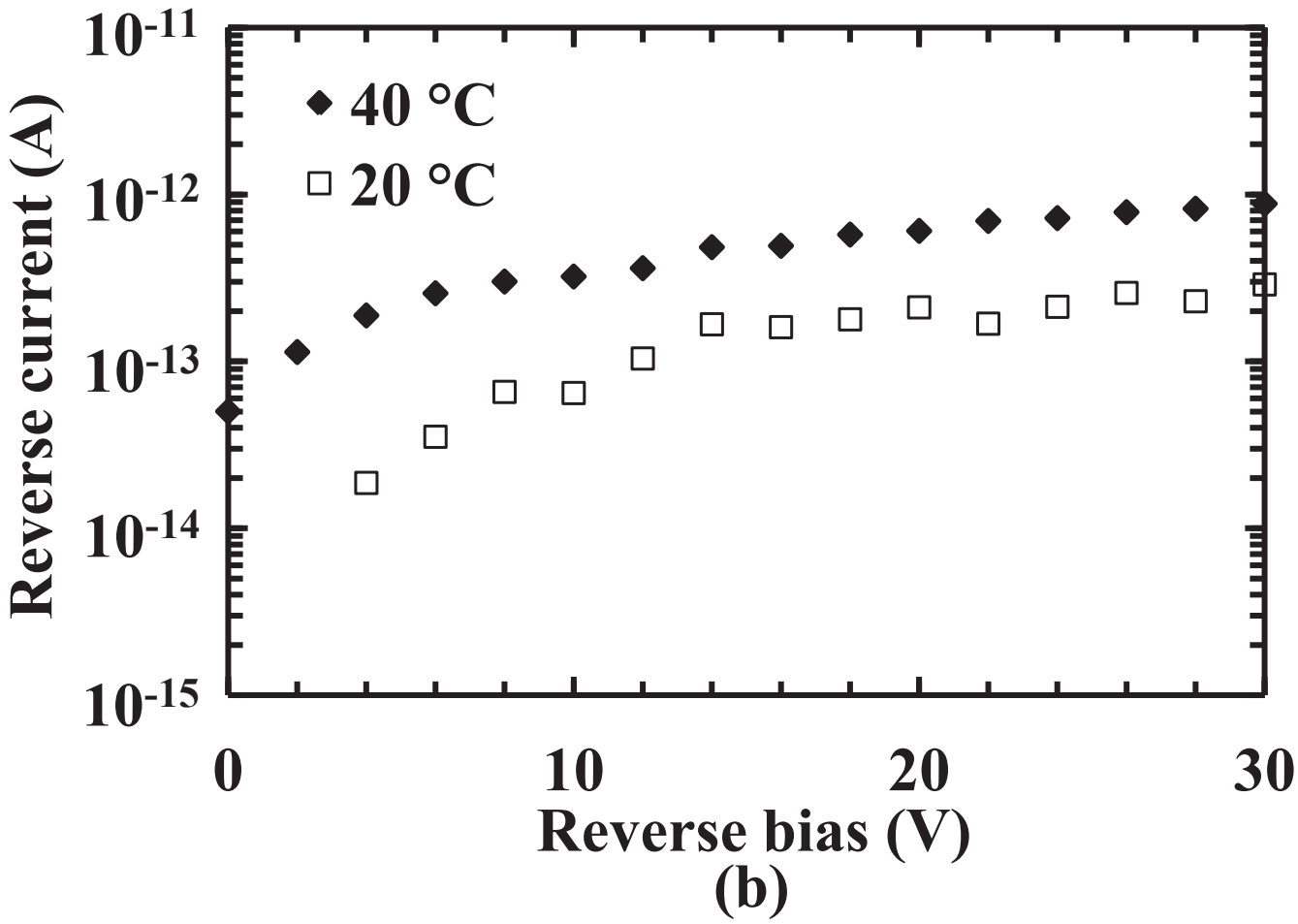
10-11
10-12
10-13
10-14
10-15
Reverse current (A)
40 °C
20 °C
0
10
20
30
Reverse bias (V)
(b)

Figure 4

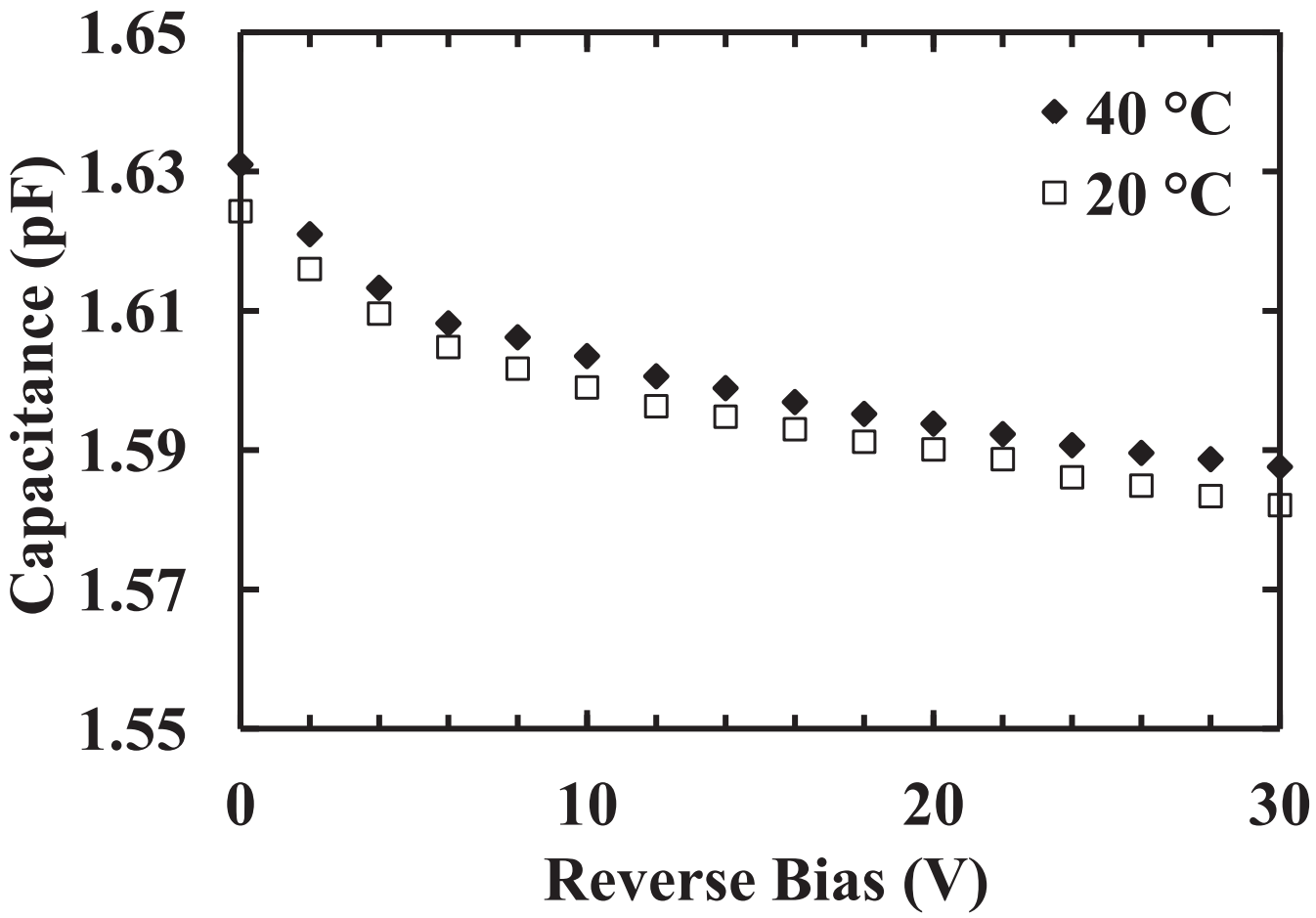
1.65
1.63
1.61
1.59
1.57
1.55
Capacitance (pF)
40 °C
20 °C
0
10
20
30
Reverse Bias (V)

Figure 5

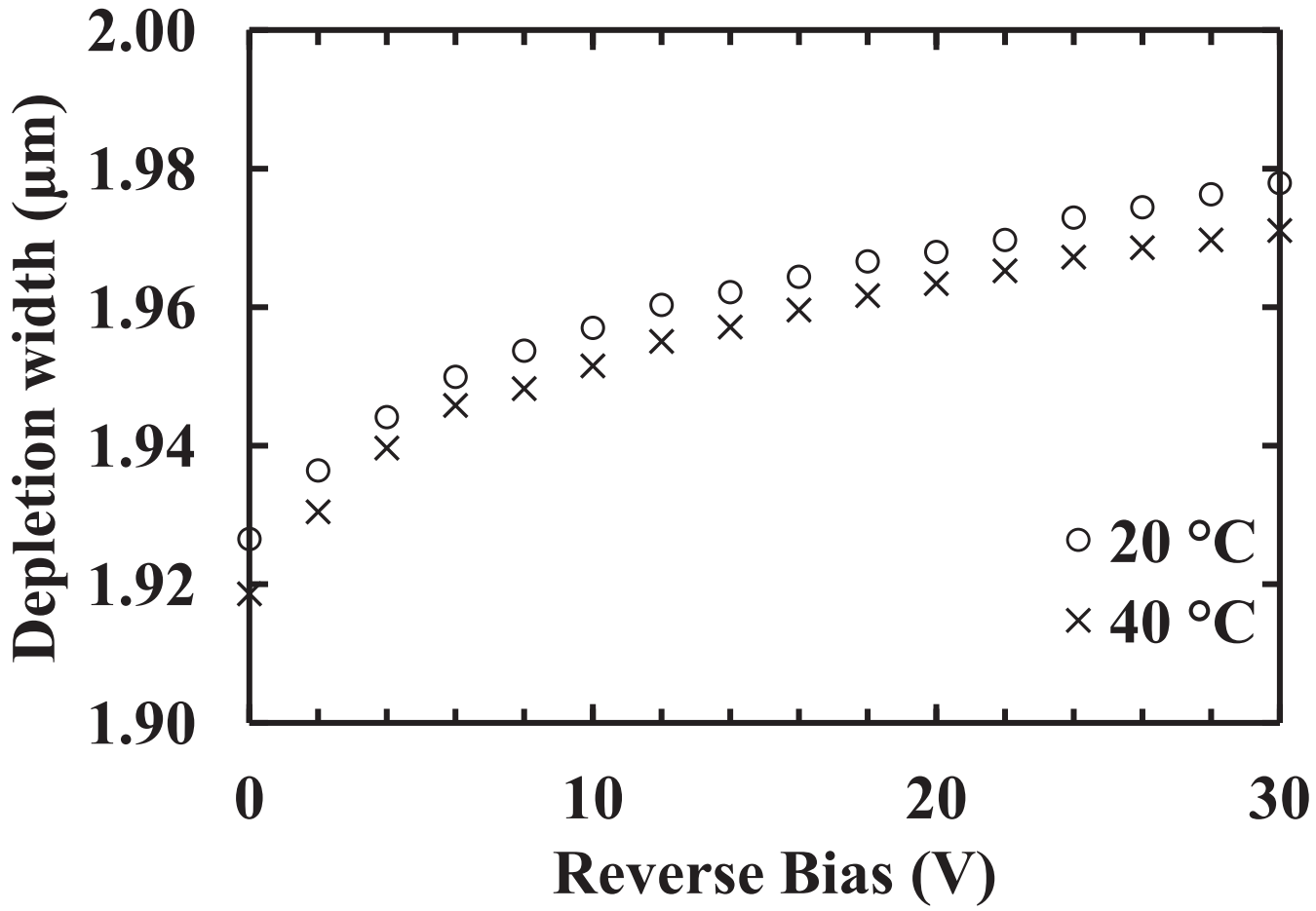
2.00
1.98
1.96
1.94
1.92
1.90
Depletion width (μm)
0
10
20
30
Reverse Bias (V)
20 °C
40 °C

Figure 6

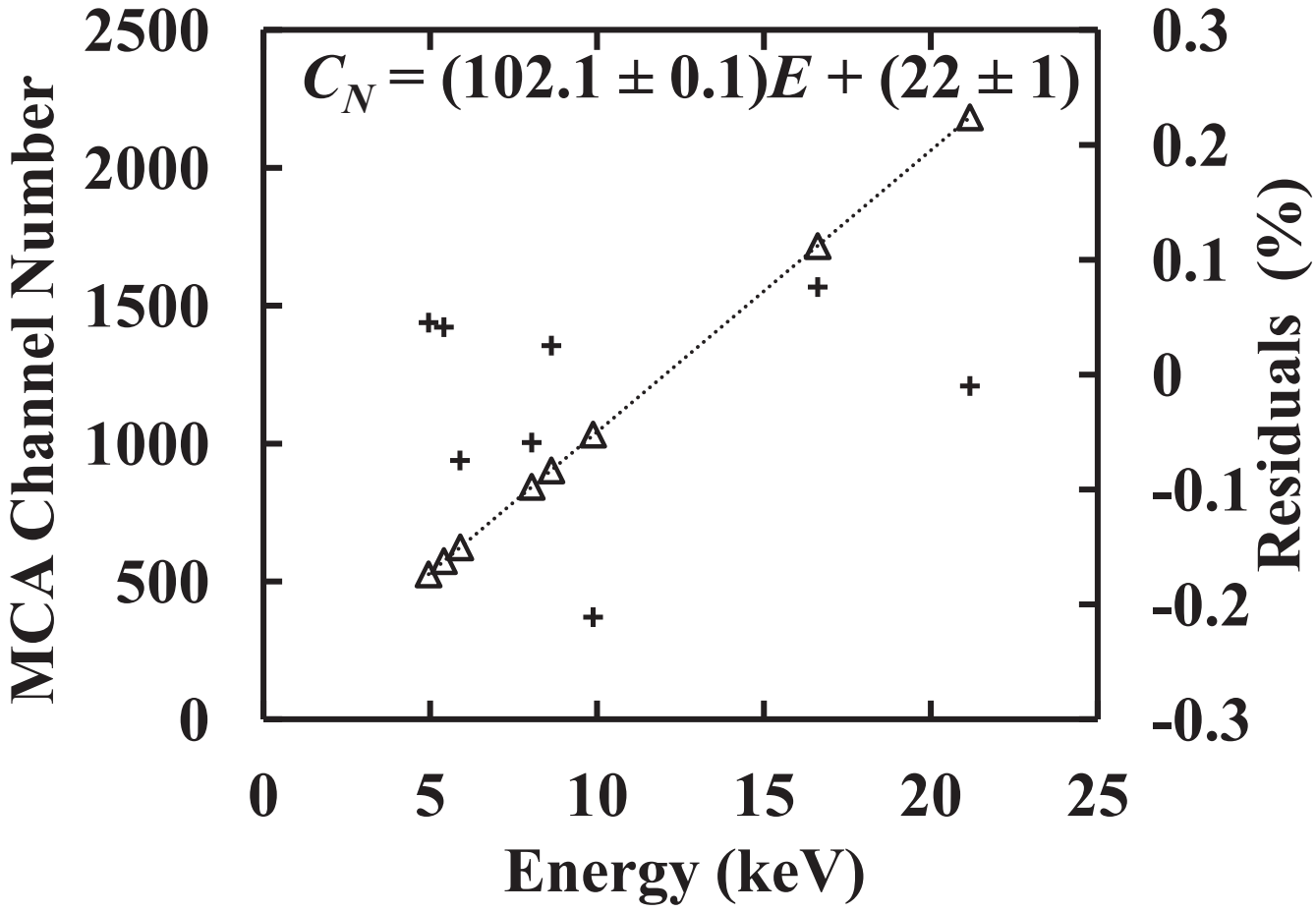
$C_N = (102.1 \pm 0.1)E + (22 \pm 1)$
MCA Channel Number
Residuals (%)
Energy (keV)
2500
2000
1500
1000
500
0
0.3
0.2
0.1
0
-0.1
-0.2
-0.3
0
5
10
15
20
25

Figure 7a

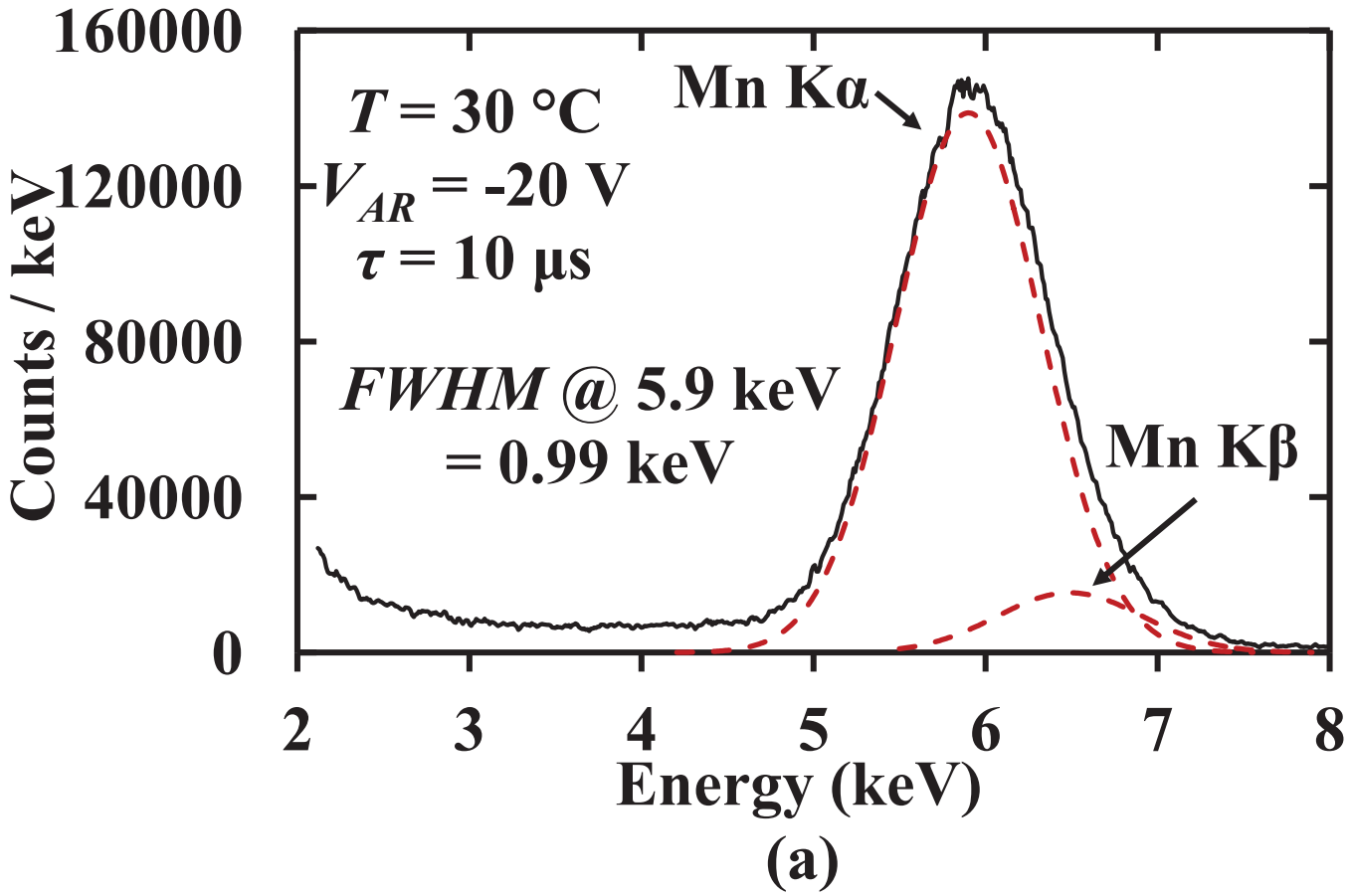
160000
120000
80000
40000
0
Counts / keV
T = 30 °C
V_AR = -20 V
τ = 10 µs
FWHM @ 5.9 keV
= 0.99 keV
Mn Kα
Mn Kβ
2
3
4
5
6
7
8
Energy (keV)
(a)

Figure 7b

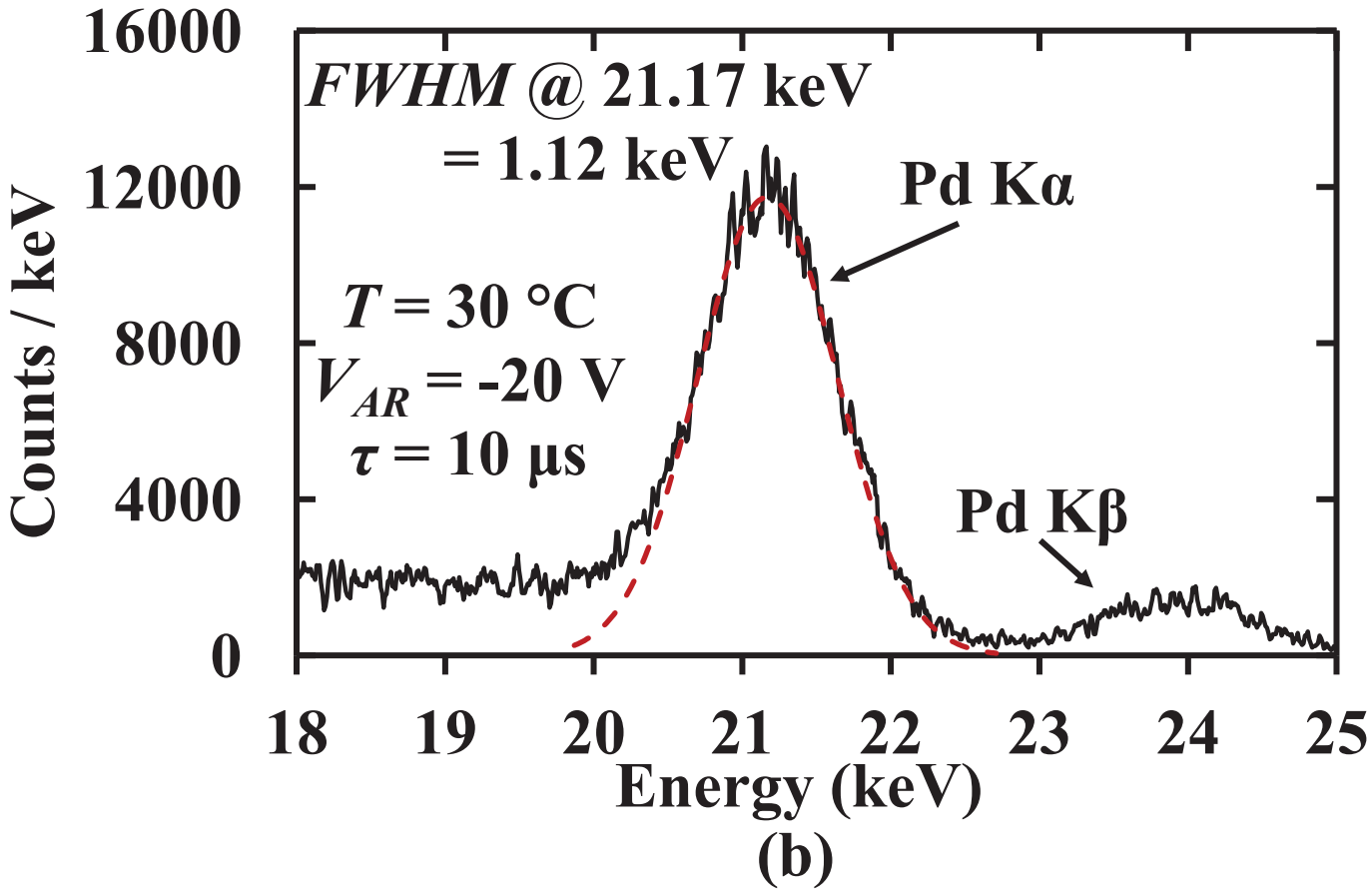
16000
12000
8000
4000
0
Counts / keV
FWHM @ 21.17 keV
= 1.12 keV
Pd Kα
T = 30 °C
V_AR = -20 V
τ = 10 µs
Pd Kβ
18
19
20
21
22
23
24
25
Energy (keV)
(b)

Figure 8

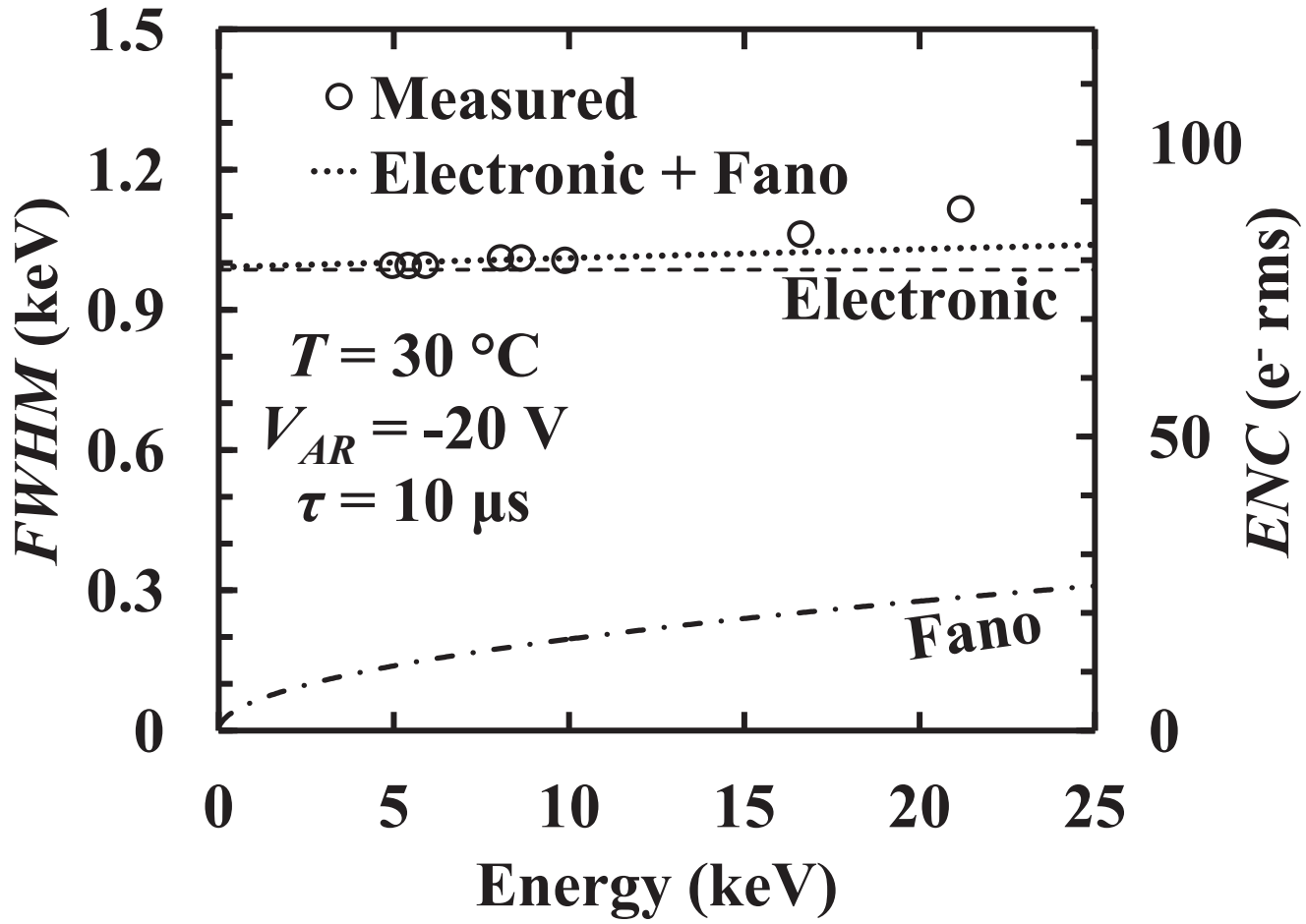
1.5
1.2
0.9
0.6
0.3
0
FWHM (keV)
Measured
Electronic + Fano
Electronic
Fano
T = 30 °C
V_AR = -20 V
τ = 10 µs
100
50
0
ENC (e- rms)
0
5
10
15
20
25
Energy (keV)

Figure 9

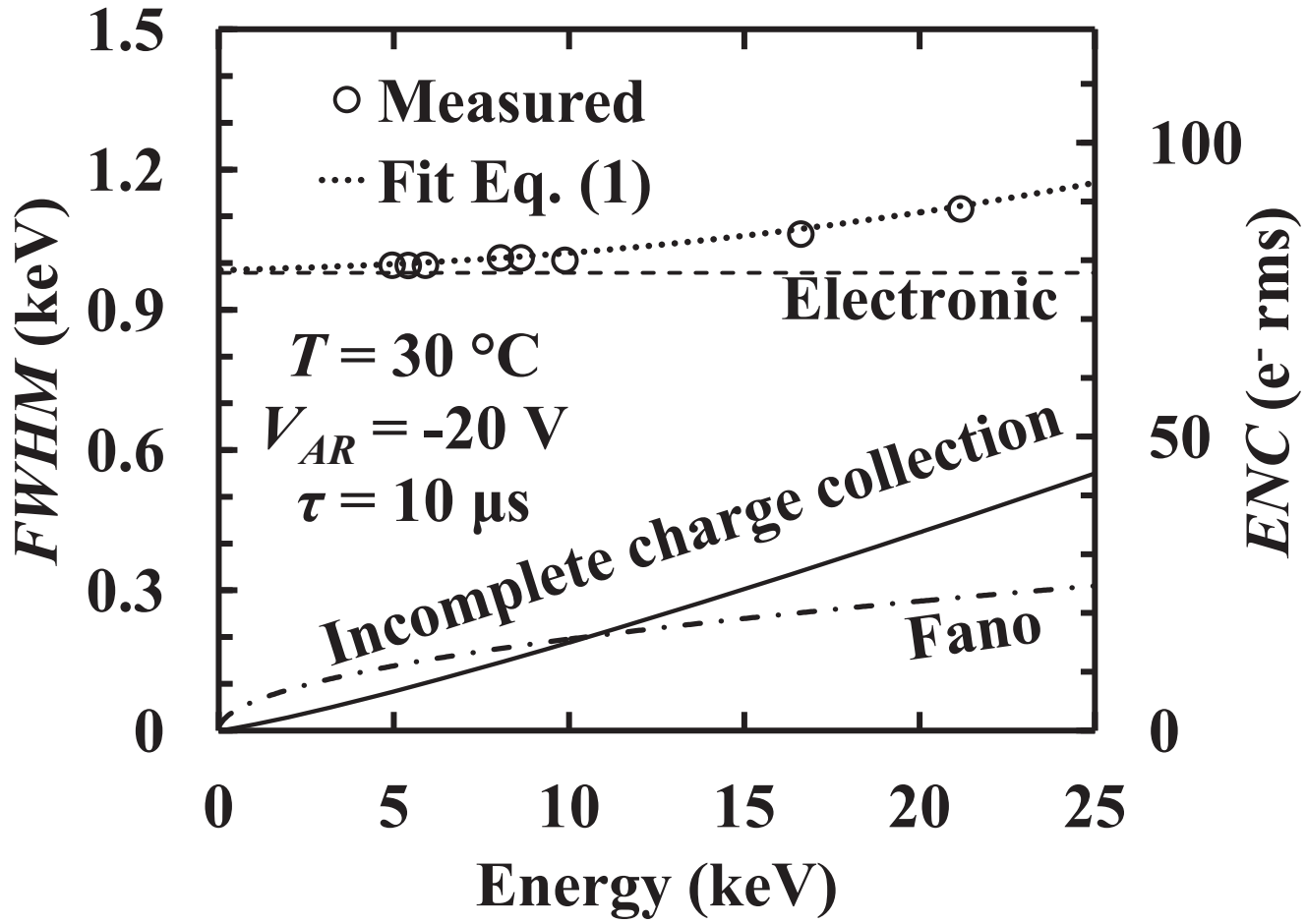
1.5
1.2
0.9
0.6
0.3
0
FWHM (keV)
100
50
0
ENC (e- rms)
Measured
Fit Eq. (1)
Electronic
T = 30 °C
V_AR = -20 V
τ = 10 µs
Incomplete charge collection
Fano
0
5
10
15
20
25
Energy (keV)

Figure 10

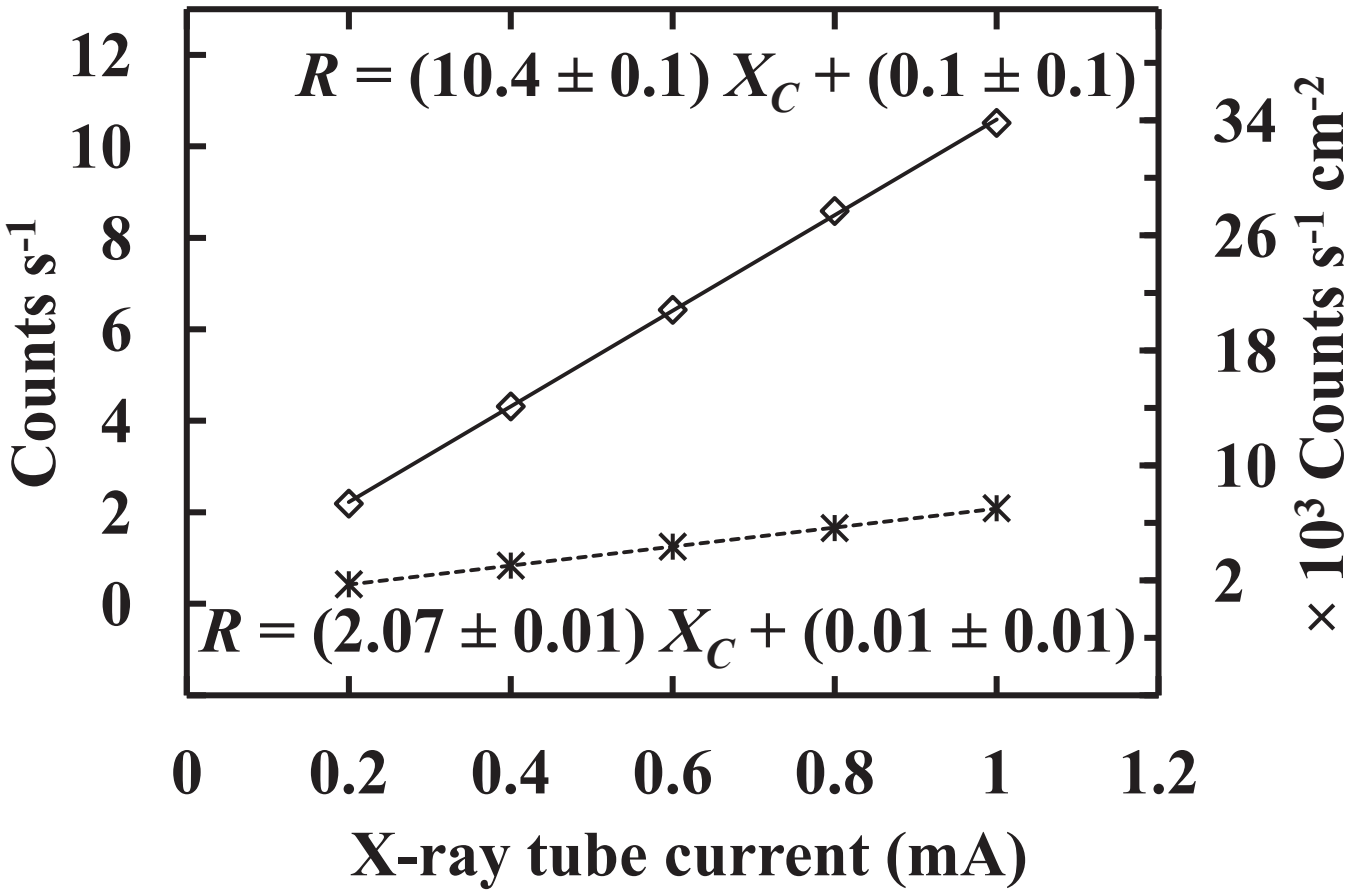
R = (10.4 ± 0.1) X_C + (0.1 ± 0.1)
R = (2.07 ± 0.01) X_C + (0.01 ± 0.01)
Counts s-1
× 10³ Counts s-1 cm-2
X-ray tube current (mA)
0
2
4
6
8
10
12
2
10
18
26
34
0
0.2
0.4
0.6
0.8
1
1.2

Figure 11

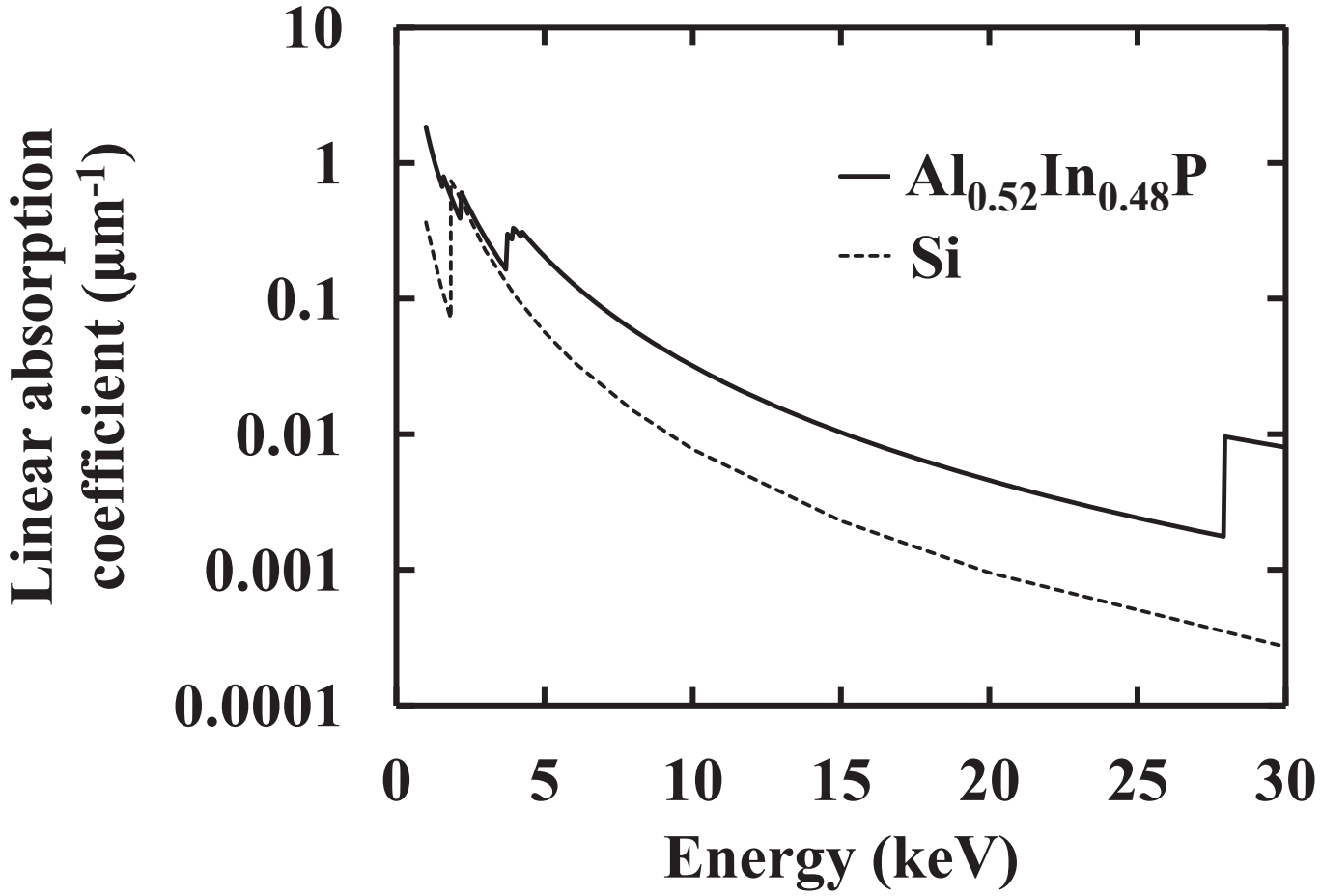
Linear absorption coefficient (μm-1)
10
1
0.1
0.01
0.001
0.0001
0
5
10
15
20
25
30
Energy (keV)
Al0.52In0.48P
Si

Table I

Material	Type	Thickness (μm)	Doping density (cm^{-3})
GaAs	p^+	0.01	1×10^{19}
$Al_{0.52}In_{0.48}P$	p^+	0.2	5×10^{17}
$Al_{0.52}In_{0.48}P$	i	2	Undoped
$Al_{0.52}In_{0.48}P$	n^+	0.1	2×10^{18}
GaAs	n^+ (substrate)		

Table II

Charge sensitive preamplifier	
Noise level (unloaded)	≈ 40 e^- rms
Input JFET V_{GS}	≈ 100 mV
Input JFET V_{DS}	≈ 5 V
Input JFET I_{DS}	≤ 10 mA
Input JFET C_i	≤ 2 pF
Input JFET g_m	≈ 4 mS
Shaping amplifier	
Fine Gain	1.437
Coarse gain	50
Shaping time	10 μs